Preliminary system for data assimilation to infer material parameters from directional solidification experiments: twin experimental study using phase-field method

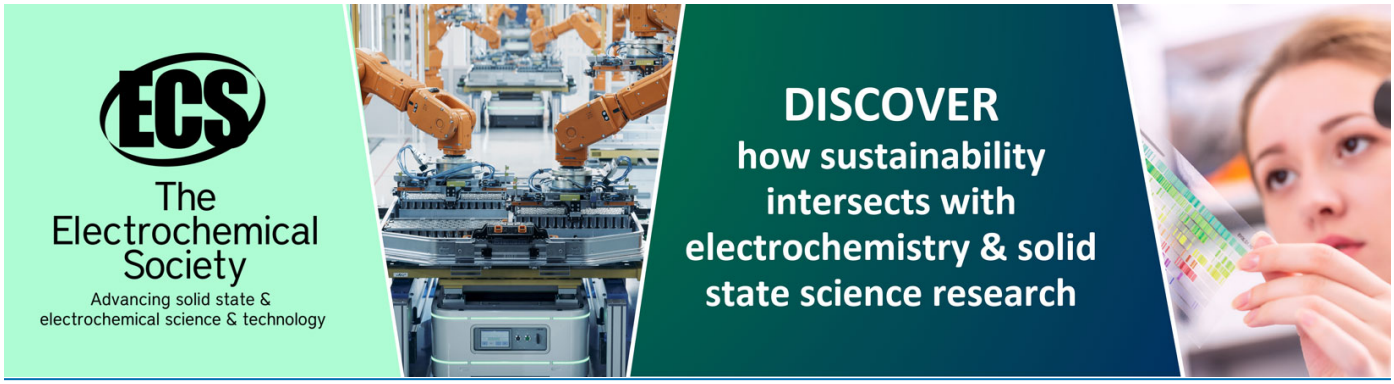

Preliminary system for data assimilation to infer material parameters from directional solidification experiments: twin experimental study using phase-field method

Y Imai[1], S Sakane[2], M Ohno[3], H Yasuda[4] and T Takaki[2]

[1] Graduate School of Science and Technology, Kyoto Institute of Technology, Matsugasaki, Sakyo-ku, Kyoto 606-8585, Japan.
[2] Faculty of Mechanical Engineering, Kyoto Institute of Technology, Matsugasaki, Sakyo-ku, Kyoto 606-8585, Japan.
[3] Division of Materials Science and Engineering, Faculty of Engineering, Hokkaido University, Kita 13 Nishi 8, Kita-ku, Sapporo, Hokkaido 060-8628, Japan.
[4] Graduate School of Engineering, University of Kyoto, Yoshidahon-machi, Sakyo-ku, Kyoto 606-8501, Japan.

takaki@kit.ac.jp

Abstract. The integration of phase-field (PF) simulations and in situ observations is a promising approach for understanding dendrite growth. In this study, a preliminary data assimilation system is developed to integrate PF simulations and in situ real-time X-ray radiography during the directional solidification of a binary alloy. In this system, only the region around the tip of a primary arm is used for data assimilation. The validity of the developed system is confirmed through twin experiments for columnar dendrite growth with different inclined angles of preferred growth direction.

1. Introduction

A highly accurate prediction of dendrite growth is essential for improving the quality of alloy products [1]. Thus, dendrite growth has been extensively investigated using numerical simulations and experiments.

The phase-field (PF) method is the most accurate model for dendrite growth. The quantitative PF models of dendrite growth [2-4], results of which do not depend on the interface thickness, are generally used for alloy solidification. However, the PF method is computationally expensive because it is a diffuse interface model. To solve this problem, an adaptive mesh refinement method and parallel computing have been applied to PF simulations [5]. Graphics processing units (GPUs) have been actively used in recent years [6], and large-scale computing has been performed using multiple GPUs in parallel [7-10]. As mentioned above, owing to the development of quantitative PF models, computational schemes, and computer hardware, the spatiotemporal domain in which the

PF method can be applied is gradually expanding. Nevertheless, the lack of material properties is a key issue in the PF simulations for dendrite solidification.

As metallic alloys are not transparent and alloy solidification occurs at high temperatures, the direct observation of dendrite growth was impossible. The time-resolved X-ray imaging of dendritic growth was proposed around 2000 [11, 12]. Time-resolved tomography (4D-CT) [13-15] has been developed in recent years, and it has advanced the understanding of dendrite growth. However, 4D-CT observations cannot be applied to fast phenomena owing to their insufficient spatiotemporal resolution, as a 3D image is created by reconstructing hundreds of transmission images obtained during the half rotation of a cylindrical specimen.

Data assimilation [16] has been attracting attention as a promising method for integrating numerical simulations and experiments. Ohno et al. developed a method for estimating interfacial properties by combining molecular dynamics and PF simulations with an ensemble Kalman filter (EnKF) and applied it to pure iron and nickel [17, 18]. Yamanaka et al. employed the local ensemble transform Kalman filter to dendritic solidification to efficiently estimate material parameters [19, 20]. Miyoshi et al. proposed a method of simultaneously inferring multiple grain boundary properties using the EnKF and multi-phase-field method [21]. However, data assimilation using actual experimental data as observation data has not yet been performed. If data assimilation can be performed using in situ observations, it will be possible to simultaneously solve the problems of spatiotemporal resolution in experiments and the material properties required in simulations. However, it is not currently feasible to perform data assimilation using PF simulations for an entire region of in situ observations because of computational costs [8].

The purpose of this study is to construct a preliminary data assimilation system to integrate in situ observations and PF simulations, where observation data is obtained only from the region around the dendrite tip of a primary arm during the directional solidification of a binary alloy to reduce the computational cost. The validity of the system is confirmed through twin experiments and two-dimensional (2D) directional solidification simulations for an Al–Cu alloy. The anisotropy strength of interfacial energy and diffusion coefficient of the liquid are simultaneously estimated.

2. Data assimilation system

In this study, the quantitative PF method for binary alloy solidification [3] was applied to directional solidification, and the EnKF [17] was used for data assimilation.

2.1. Phase-field method

The PF variable, ϕ, is defined as $\phi = 1$ in the solid phase and $\phi = -1$ in the liquid phase, and ϕ varies smoothly from 1 to –1 at the interface. The evolution equation of ϕ is given by

$$t\left[1-(1-k)u'\right]\frac{\partial f}{\partial t}=\nabla\cdot\left[W^2\nabla f\right]+\sum_{i=x,y}\left[W\frac{\partial W}{\partial f_i}\left|\nabla f\right|^2\right]-f\left(f^2-1\right)-l^*\left(1-f^2\right)^2(u+u') \tag{1}$$

where τ is the relaxation time of ϕ and W is the interface thickness; $\tau = \tau_0 a_s(\nabla\phi)^2$ and $W = W_0 a_s(\nabla\phi)$. The anisotropy function is $a_s(\nabla\phi) = 1 - 3\varepsilon_4 + 4\varepsilon_4(\phi_x^4 + \phi_y^4) / |\nabla\phi|^4$, and ε_4 is the anisotropy strength of interfacial energy. ϕ_i denotes the partial derivative of ϕ with respect to i. λ^* is the quantity associated with the thermodynamic driving force. u is dimensionless supersaturation, which is expressed as $u = (c_l - c_l^e)/(c_l^e - c_s^e)$. c_l is the liquid concentration, and c_l^e and c_s^e are the equilibrium concentrations in the liquid and solid, respectively. The temperature change is expressed as $T(y) = T_0 + G(y - Vt)$ by

applying the frozen temperature approximation, where T_0 is the temperature at $y = 0$ and $t = 0$, G is the temperature gradient in the y-direction, and V_p is the pulling velocity. u' in equation (1) is expressed as $u' = (y - Vt)/l_T$ using thermal length l_T. The time evolution equation of u is given by

$$\frac{[1+k-(1-k)\phi)]}{2}\frac{\partial u}{\partial t} = \nabla[D_l q(\phi)\nabla u - j_{AT}] + \frac{1}{2}[1+(1-k)u]\frac{\partial \phi}{\partial t} \quad (2)$$

where $q(\phi) = [kD_s + D_l + (kD_s - D_l)\phi] / (2D_l)$, k is the partition coefficient, and D_l and D_s are the diffusion coefficients of the liquid and solid phases, respectively. j_{AT} is the antitrapping term, which is added to perform quantitative calculations independent of the interface width.

2.2. Data assimilation

A sequential data assimilation system that uses the EnKF was developed in this study. The EnKF can be applied to nonlinear system models such as the PF equation. The probability distribution of state vector $\boldsymbol{x}_t$ containing unknown parameters is represented by a set, $\{\boldsymbol{x}_t^{(i)}\}_{i=1}^{N}$, of N state vectors. This is referred to as the ensemble approximation, where N is ensemble members. The state vector of i-th ensemble member at time t is expressed by $\boldsymbol{x}_t^{(i)} = \{\boldsymbol{\phi}_t^{(i)}\ \boldsymbol{u}_t^{(i)}\ \varepsilon_{4,t}^{(i)}\ D_{l,t}^{(i)}\}^{\mathrm{T}}$, where $\boldsymbol{\phi}_t^{(i)}$ and $\boldsymbol{u}_t^{(i)}$ are the vectors of ϕ and u at all grid points at time t, respectively. ε_4 and D_l are estimated in the twin experiments and included in the ensemble member as unknown parameters. $\boldsymbol{x}_t^{(i)}$ is updated by repeating the prediction and filtering, and the unknown parameters are expected to gradually approach the true values in this process. The prediction is based on the following system model:

$$\boldsymbol{x}_{t|t-1}^{(i)} = f_t\left(\boldsymbol{x}_{t-1}^{(i)}\right) + \boldsymbol{v}_t^{(i)} \tag{3}$$

where subscript $t|t$–1 in $\boldsymbol{x}_{t|t-1}^{(i)}$ indicates the values at time t obtained using the values at time $t-1$. f_t is a nonlinear map from $\boldsymbol{x}_{t-1}$ to $\boldsymbol{x}_t$, and it corresponds to equations (1) and (2). $\boldsymbol{v}_t^{(i)}$ is system noise, which follows a Gaussian distribution with mean vector $\mathbf{0}$ and variance–covariance matrix $\boldsymbol{Q}_t$. $\boldsymbol{v}_t^{(i)}$ is used to express the uncertainty of numerical simulation. The state vector is updated at every time step in the simulation with time increment Δt on the basis of equation (3). At time $t = n\Delta t_{obs}$, when observed data are available, the state vector is updated by filtering with the following equation:

$$\boldsymbol{x}_{t|t}^{(i)} = \boldsymbol{x}_{t|t-1}^{(i)} + \boldsymbol{K}_t[\boldsymbol{y}_t + \breve{\boldsymbol{w}}_t^{(i)} - \boldsymbol{H}_t\boldsymbol{x}_{t|t-1}^{(i)}] \tag{4}$$

where $\boldsymbol{K}_t$ is the Kalman gain, which determines the degree of correction of the state vector on the basis of the observation data. It is computed as $\boldsymbol{K}_t = \boldsymbol{V}_t\boldsymbol{H}_t^{\mathrm{T}}(\boldsymbol{H}_t\boldsymbol{V}_t\boldsymbol{H}_t^{\mathrm{T}} + \boldsymbol{R}_t)^{-1}$, where $\boldsymbol{V}_t = (N-1)^{-1}\sum_{j=1}^{N}\breve{\boldsymbol{x}}_t^{(j)}\breve{\boldsymbol{x}}_t^{(j)\mathrm{T}}$ and $\breve{\boldsymbol{x}}_t^{(j)} = \boldsymbol{x}_{t|t-1}^{(j)} - N^{-1}\sum_{j=1}^{N}\boldsymbol{x}_{t|t-1}^{(j)}$. Observation matrix $\boldsymbol{H}_t$ is computed from the observation model, $\boldsymbol{y}_t = \boldsymbol{H}_t\boldsymbol{x}_{t|t-1}^{(i)} + \boldsymbol{w}_t^{(i)}$, and observation noise $\boldsymbol{w}_t^{(i)}$ follows a Gaussian distribution with mean vector $\mathbf{0}$ and variance–covariance matrix $\boldsymbol{R}_t$. In equation (4), $\breve{\boldsymbol{w}}_t^{(i)}$ is expressed as $\breve{\boldsymbol{w}}_t^{(i)} = \boldsymbol{w}_t^{(i)} - N^{-1}\sum_{j=1}^{N}\boldsymbol{w}_t^{(j)}$, and $\boldsymbol{y}_t + \breve{\boldsymbol{w}}_t^{(i)}$ is referred to as the disturbed observation. For simplicity, we consider $\boldsymbol{R}_t = \sigma_r^2\boldsymbol{I}$ with variance σ_r^2, covariance $\mathbf{0}$, and unit matrix $\boldsymbol{I}$.

Table 1. Material properties of Al–3wt%Cu and simulation conditions for obtaining observation data. "*" denotes artificially determined values.

Parameter	Symbol	Value
Initial concentration	C_0	0.013 at.frac.
Melting point of pure Al	T_m	933.25 K
Partition coefficient	k	0.14
Anisotropic strength	ε_4	0.009 *
Gibbs–Thomson coefficient	Γ	0.24×10^{-6} Km
Diffusion coefficient in liquid	D_l	2.0×10^{-9} m^2/s *
Diffusion coefficient in solid	D_s	2.0×10^{-13} m^2/s *
Liquidus slope	m	-620 K/at.frac
Temperature gradient	G	100 K/mm
Pulling velocity	V_p	100 μm/s

Computational domain size	$L_x \times L_y$	$1000 \times 6000\Delta x^2$
Grid size	Δx	0.4 μm
Interface thickness	W_0	$\Delta x/0.6$
Time increment	Δt	1.6×10^{-5} s

3. Observation data

The 2D directional solidification PF simulations of Al–3wt%Cu were carried out to generate observation data for the twin experiments. The material properties and calculation conditions are listed in table 1. ε_4 and D_l were set to assumed values and these values will be estimated in the EnKF. The simulations were performed for two different preferred growth directions with θ = 0° and θ = 15°, where θ is the angle between the preferential growth direction and temperature gradient direction (y-axis). As the initial conditions, the entire computational domain was filled with a liquid phase with u_0 = -0.295, and a semicircular solid with radius $6\Delta x$ was placed at the center of the bottom of the computational domain. Figures 1(a) and (b) depict the simulation results for θ = 0° and θ = 15°, respectively. Typical columnar dendrites grew in the temperature gradient direction with secondary arms.

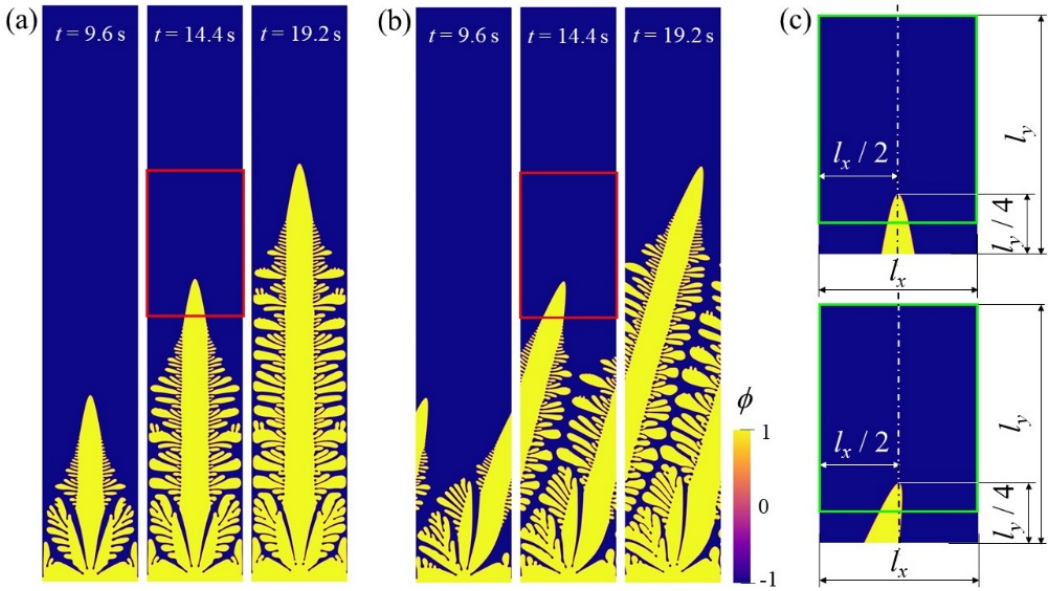

Figure 1. Time evolution of dendrite morphology for (a) θ = 0° and (b) θ = 15°. (c) Dendrite tip regions enclosed by rectangular red regions in (a) and (b), which correspond to the simulation domain in prediction of data assimilation. The rectangular green regions were used for filtering.

Table 2. Parameters used in the twin experiments.

Parameter	Symbol	Value
Ensemble size	N	100
Variance of observation noise	σ_r^2	1.0
Initial value of ε_4	$\varepsilon_{4,\,init}$	0.005
Initial standard deviation of ε_4	$\sigma_{\varepsilon 4,\,init}$	$0.5 \times \varepsilon_{4,\,init}$
Initial value of D_l	$D_{l,\,init}$	1.0×10^{-9}
Initial standard deviation of D_l	$\sigma_{Dl,\,init}$	$0.25 \times D_{l,\,init}$
Variance of system noise for ϕ	σ_ϕ^2	1.0×10^{-6}
Variance of system noise for u	σ_u^2	1.0×10^{-8}

Variance of noise for ε_4	$\sigma_{\varepsilon 4}^2$	1.0×10^{-11}
Variance of noise for D_l	σ_{Dl}^2	1.0×10^{-23}

4. Twin experiments

ε_4 and D_l were inferred through the twin experiments to confirm the validity of the developed data assimilation system. We used only the region around the dendrite tip of the primary arm to reduce the computational cost of data assimilation. The size of the region was set to $l_x \times l_y = 400 \times 600$ μm^2 ($1000 \times 1500 \Delta x^2$) so that the solute diffusion field in front of the dendrite tip did not reach the upper edge of the region. The rectangular red regions were extracted from the results presented in figure 1 so that the dendrite tip was always positioned at ($l_x/2$, $l_y/4$). For $\theta = 15°$, the domain was shifted in the lateral direction such that the tip position was ($l_x/2$, $l_y/4$). We obtained 50 data of microstructure (ϕ profile) during t = 14.4 s–15.2 s as the observation data. Thus, the time increment of the observation data was Δt_{obs} = 0.016 s. As the explicit scheme was used for the time derivatives of equations (1) and (2), the time increment changed depending on D_l. Hence, the maximum value of D_l was set as 4.0×10^{-9} m/s^2, which was twice the true value presented in table 1, and the time increment was set as 0.8×10^{-5} s. The PF simulations during data assimilation were carried out using a moving frame algorithm to maintain the dendrite tip position at ($l_x/2$, $l_y/4$) using the region illustrated in figure 1(c). For $\theta = 15°$, the lateral motion of the region was also introduced to maintain the dendrite tip position at ($l_x/2$, $l_y/4$). The boundary conditions were set as periodic on the left and right sides and zero Neumann on the top and bottom. When the moving frame algorithm is used in a small region, as depicted in figure 1(c), the solidification morphology at the lower end of the region may be destabilized by the zero-Neumann condition. Therefore, data assimilation was performed in the green frame, which did not include the lower edge. Observation vector $\boldsymbol{y}_t$ was set as $\boldsymbol{y}_t = \boldsymbol{\phi}_t^{obs}$. The other conditions for data assimilation are listed in table 2.

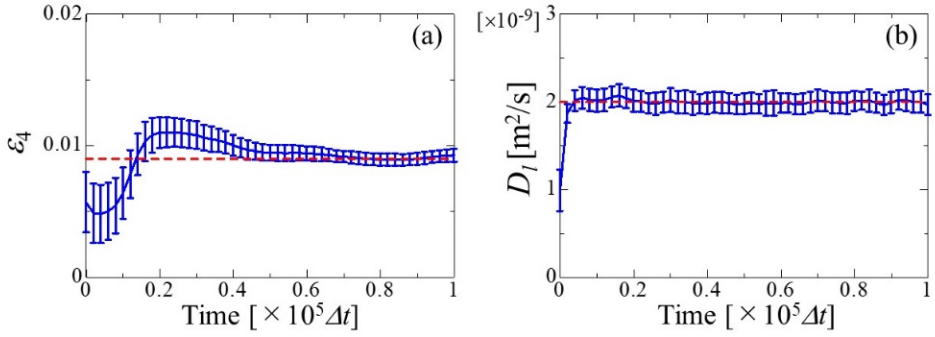

Figure 2. Inference results obtained during data assimilation for (a) anisotropy strength of interfacial energy, ε_4, and (b) diffusion coefficient of liquid, D_l, for the observation data for $\theta = 0°$.

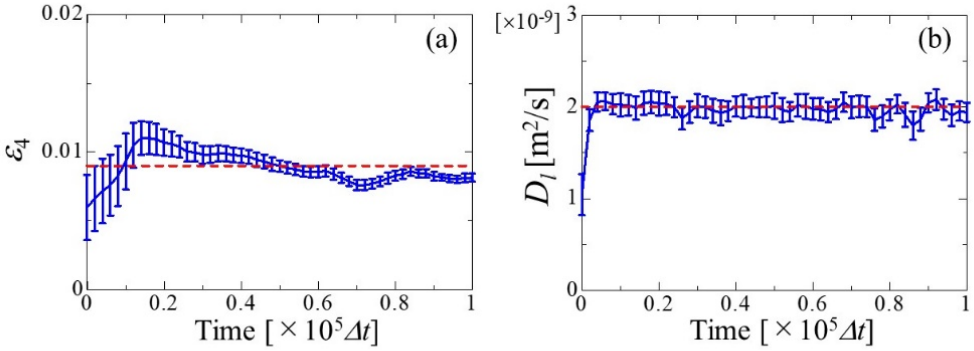

Figure 3. Inference results obtained during data assimilation for (a) anisotropy strength of interfacial energy, ε_4, and (b) diffusion coefficient of liquid, D_l, for the observation data for $\theta = 15°$.

Figure 2 presents the inference results of ε_4 and D_l for $\theta = 0°$. The red dashed line represents the true value, the blue line represents the change in the estimated average value, and the error bars represent the standard deviation of the estimated values. D_l rapidly approached the true value from the initial value, and the approximate true value was estimated in the second filtering. In contrast, the inferred value of ε_4 approached the true value in approximately the 40th filtering. The difference between the convergence behaviors of ε_4 and D_l depended on their contribution to the dendrite tip shape. Although ε_4 and D_l affected the tip morphology of the dendrite, the effect of D_l was stronger than that of ε_4. Nevertheless, we successfully inferred ε_4 and D_l simultaneously using the developed data assimilation system.

Figure 3 presents the inference results of ε_4 and D_l for $\theta = 15°$. The tendency of the convergence behaviors of ε_4 and D_l was similar to that illustrated in figure 2. However, the fluctuations for $\theta = 15°$ were larger than those for $\theta = 0°$. In addition, the convergence of ε_4 to the true value was comparatively slower for $\theta = 15°$. As illustrated in figure 1, when the rectangular red regions were extracted, the data was converted such that the position of the dendrite tip was (l_x/2, l_y/4). Subsequently, the data was shifted to a unit of the grid size. In addition, the moving frame algorithm in the PF simulations was applied in a unit of the grid size. These migrations in the x-direction caused the error in the inference of ε_4 for $\theta = 15°$. In other words, the effect of the deviation of the interface position between the observation data and simulations was stronger for ε_4 compared to that for D_l. Nevertheless, the estimation accuracy was less than 10%, even for ε_4. Thus, the estimation was highly accurate even when the dendrite was inclined.

5. Conclusions

A preliminary data assimilation system was developed to integrate PF simulations and in situ real-time X-ray radiography during the directional solidification of a binary alloy. Observation data were obtained from the region around the tip of a primary arm to reduce the computational cost. The validity of the developed system was confirmed through twin experiments of the 2D directional solidification of an Al–Cu alloy with different inclined angles of the dendrite. In future work, we will apply the proposed system to the time-resolved X-ray imaging of dendritic growth during directional solidification.

Acknowledgement

This work was supported by KAKENHI, Grant-in-Aid for Scientific Research (A) 20H00217.

References

[1] Dantzig J A and Rappaz M 2009 *Solidification*: EFPL Press)
[2] Karma A and Rappel W J 1998 *Physical Review E - Statistical Physics, Plasmas, Fluids, and Related Interdisciplinary Topics* **57** 4323-49
[3] Ohno M and Matsuura K 2009 *Physical Review E* **79** 031603
[4] Ohno M 2020 *ISIJ International* **60** 2745-54
[5] Sakane S, Takaki T and Aoki T 2022 *Materials Theory* **6** 3
[6] Karma A and Tourret D 2016 *Current Opinion in Solid State and Materials Science* **20** 25-36
[7] Shibuta Y, Ohno M and Takaki T 2015 *JOM* **67** 1793-804
[8] Shibuta Y, Ohno M and Takaki T 2018 *Advanced Theory and Simulations* **1** 1800065

[9] Takaki T, Sakane S, Ohno M, Shibuta Y and Aoki T 2022 *Computational Materials Science* **203** 111143
[10] Takaki T, Sakane S, Ohno M, Shibuta Y and Aoki T 2020 *Computational Materials Science* **171** 109209
[11] Mathiesen R H, Arnberg L, Mo F, Weitkamp T and Snigirev A 1999 *Physical Review Letters* **83** 5062-5
[12] Yasuda H, Ohnaka I, Kawasaki K, Sugiyama A, Ohmichi T, Iwane J and Umetani K 2004 *Journal of Crystal Growth* **262** 645-52
[13] Ludwig O, Dimichiel M, Salvo L, Suéry M and Falus P 2005 *Metallurgical and Materials Transactions A* **36** 1515-23
[14] Puncreobutr C, Phillion A B, Fife J L and Lee P D 2014 *Acta Materialia* **64** 316-25
[15] Yasuda H, Kawarasaki T, Tomiyori Y, Kato Y and Morishita K 2019 Characterization of dendritic growth in Fe-C system using time-resolved X-ray tomography and physics-based filtering. In: *IOP Conference Series: Materials Science and Engineering,*
[16] Houtekamer P L and Zhang F 2016 *Monthly Weather Review* **144** 4489-532
[17] Ohno M, Oka Y, Sakane S, Shibuta Y and Takaki T 2020 *Physical Review E* **101** 052121
[18] Nagatsuma Y, Ohno M, Takaki T and Shibuta Y 2021 *Nanomaterials* **11** 2308
[19] Yamanaka A and Takahashi K 2020 *Materials Today Communications* **25** 101331
[20] Takahashi K and Yamanaka A 2021 *Computational Materials Science* **190** 110296
[21] Miyoshi E, Ohno M, Shibuta Y, Yamanaka A and Takaki T 2021 *Materials & Design* **210** 110089